THE JOURNAL OF PHYSICAL CHEMISTRY C
A JOURNAL OF THE AMERICAN CHEMICAL SOCIETY

pubs.acs.org/JPCC

Article

In Situ TEM Study of the Genesis of Supported Nickel Catalysts

Savannah J. Turner, Dennie F. L. Wezendonk, Robert J. A. M. Terorde, and Krijn P. de Jong*

Cite This: J. Phys. Chem. C 2023, 127, 7772−7783

Read Online

ACCESS | Metrics & More | Article Recommendations | Supporting Information

ABSTRACT: *In situ* transmission electron microscopy is a powerful technique with the unique ability to temporally and spatially resolve nanoscale processes. This can be leveraged in order to obtain insight into the timescales of phenomena occurring during particle growth during the preparation of supported metal catalysts. Thanks to careful experimental design and comparison with *ex situ* results, the growth of individual nickel nanoparticles from a nickel phyllosilicate catalyst precursor during reduction was studied *in situ* under atmospheric pressure of 5% H2/Ar at 500 °C and modeled with first-order reaction kinetics. Particles grew rapidly, reaching a final size of between 3.5 and 7 nm within 3−4 min. The vast majority of particles grow as immobile single particles. A two-step particle growth mechanism was sometimes observed wherein two particles nucleating sufficiently close to one another sintered. The resulting particles were not significantly larger (5−7 nm) than those that did not undergo this sintering process. This finding supports the hypothesis that the size of the region from which the nickel species originated determined the particle size.

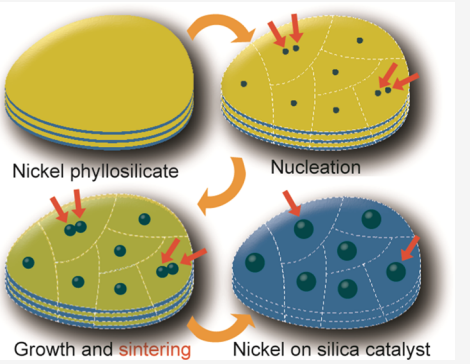

1. INTRODUCTION

Developing an understanding of the mechanisms of particle growth on the nanoscale is highly valuable to the field of catalyst preparation. The primary aim of the study of the synthesis of supported metal catalysts is to optimize their activity and selectivity. These parameters are determined by factors such as particle size, shape, and distribution across the support.[1−3] These properties are dependent on the conditions of the synthesis and therefore the mechanism of the nanoparticle formation. Enhanced understanding of particle formation and growth mechanisms enables the tailoring of catalyst synthesis conditions and therefore the optimization of the activity and selectivity of the catalyst toward specific reactions.

For many industrially relevant catalysts, the catalytically active nanoparticles are formed during the reduction step. Industrial catalysts are commonly prepared using techniques such as deposition precipitation and coprecipitation.[4−6] The principle behind precipitation techniques is to deposit a metal onto an inert support material by converting a soluble metal precursor to an insoluble form. The insoluble compounds deposited on the support are often inactive for catalysis (such as metal hydroxides, oxides, or silicates) and as such are termed catalyst precursors.[7−9] Activation processes, commonly consisting of heat treatments such as calcination and reduction, convert the catalyst precursors into active catalysts. Reduction involves the conversion of the metal oxide or silicate into the reduced metallic state; thus, it is in this step that the catalytically active nanoparticles nucleate and grow. The conditions under which this step is performed are crucial in determining the size, shape, and distribution of the particles.[10,11] Understanding the mechanism of particle formation and growth during reduction is fundamental to controlling these properties and therefore the eventual performance of the catalyst.

Unfortunately, knowledge on the details such as the mechanism and kinetics of the particle formation and growth on the nanoscale is limited.[12] Many studies make use of bulk information obtained from techniques such as temperature-programmed reduction (TPR), and thermogravimetric analysis (TGA) in combination with choices of appropriate standard particle nucleation and growth mechanism models (eg. LaMer model) to determine the kinetic parameters of reduction processes.[13,14] The choice of particle nucleation and growth models are predominantly based on postmortem ex situ analysis of particle size distributions obtained by transmission electron microscopy (TEM).[15] This method of studying catalyst nanoparticle growth during reduction relies on correct guesses being made about the mechanism through which the particles grow, and assumes that the bulk reduction kinetics directly correlate with the particle growth kinetics. There is a notable shortage of techniques that enable the study of nanoparticle growth kinetics and mechanisms directly at the nanoscale.[16]

Received: February 17, 2023
Revised: April 5, 2023
Published: April 18, 2023

Transmission electron microscopy is a powerful technique capable of providing the required detailed nanostructural information on the size, composition, phase, strain, and morphology of the catalyst particles.[17] The drawback of this technique has always been the requirement that samples be observed under ultrahigh-vacuum conditions, limiting the technique to *ex situ* analysis of samples. Environmental TEM, wherein the microscope is modified in order to enable the introduction of low pressures of gasses (most commonly up to 4 mbar) in the vicinity of the sample, has historically been used to initiate investigations into nanoparticle growth mechanisms.[18−20] Recent developments in *in situ* electron microscopy now enable the introduction of gasses at atmospheric pressure into the electron microscope by sandwiching the gas layer between two electron transparent silicon nitride chips to form a microreactor.[21−24] This allows pressures of up to 1 bar to be achieved as well as controlled gas flow rates during imaging. New silicon-carbide-based heating membranes also allow for less temperature drift and therefore more stable imaging across a wide range of temperatures. It is therefore now possible to approach the conditions of *ex situ* reactors in the laboratory inside the electron microscope.[25] With careful evaluations of beam effects and hydrodynamic differences, more insight into processes such as the growth of particles in supported metal catalysts is finally within reach thanks to *in situ* TEM.[26]

In this study, the particle formation and growth during the reduction of a nickel-phyllosilicate-based catalyst precursor prepared by a common deposition precipitation technique was investigated using *in situ* gas-phase TEM. The growth of individual nanoparticles was tracked on the nanoscale providing information on the particle growth mechanisms with unprecedented details.

2. METHODS

2.1. Synthesis of Nickel Phyllosilicate. Nickel phyllosilicate was synthesized by deposition precipitation using the urea hydrolysis method as described in the literature.[7,27,28] A mass of 6.1 g of silica (Aerosil OX50) was added to a five-neck 500 mL baffled flask, then 15.2 g of nickel nitrate hexahydrate (Sigma-Aldrich) was dissolved in 350 mL of distilled water, added to the flask and stirred vigorously. An overhead stirrer was introduced through the central neck of the flask, and two others were used to monitor the reaction with a thermometer and pH meter. The two remaining necks of the flask were sealed with stoppers; however, the space between the pH meter, the thermometer, and the overhead stirrer bar and the necks of the flask were not sealed and therefore evaporation could occur as well as loss of CO_2 gas formed during the decomposition of the urea. The contents of the flask were then heated to 90 °C and acidified with a few drops of HNO_3 to a pH of 2−3. A solution of 9.4 g of urea dissolved in a further 100 mL of water was added to the flask and the pH and temperature were measured continuously throughout the experiment. The temperature was maintained at between 87 and 92 °C and after an initial rise in pH it stabilized at around 5.4. The level of the water was regularly topped up with small amounts of water added by a pipette to the flask to compensate for evaporation and keep the liquid volume constant. After 4 h of reaction, the green phyllosilicates were filtered, washed with water until the filtrate ran clear, and then dried in a static air oven at 120 °C overnight. A mass of approximately 2.5 g of the as-synthesized material was calcined in a tube furnace at 400 °C with a ramp of 5 °C·min^{-1} under a flow of Argon for 2 h. To prepare the reduced sample, 1 g of the calcined sample in powder form was reduced in the same tube furnace under 5% H_2/Ar at 500 °C (ramp of 5 °C·min^{-1}) for 2 h. The sample was then passivated by exposing it to a small amount of diluted air by creating a small leak in the flow of argon.

2.2. Characterization. X-ray diffraction (XRD) measurements were performed on a Bruker-AXS D2 Phaser X-ray diffractometer equipped with a Lynxeye detector (Co Kα1,2, λ = 1.790 Å) in Bragg−Brentano mode. Samples were prepared as flat plates from ground powder. Diffractograms were acquired between 20 and 80° 2θ, while the sample was rotated at a rate of 15 rpm.

Nitrogen physisorption isotherms were measured on a Micromeritics TriStar II Plus device at −196 °C. The samples were dried overnight under a N_2 flow at 300 °C before the measurement. The Brunauer−Emmett−Teller (BET) method was used to ascertain the surface area by curve fitting at monolayer adsorption.

Temperature-programmed reduction (TPR) by H_2 was performed on a Micromeritics AutoChem II 2920 apparatus. Nickel phyllosilicate (21 mg sieve fraction 35−300 μm) was dried at 120 °C under a flow of 50 mL·min^{-1} of Ar for 15 min. The sample was allowed to cool to room temperature, then was heated under 5% H_2/Ar flow of 25 mL·min^{-1} with 10 °C·min^{-1} up to 900 °C. Reduction profiles were recorded with a thermal conductivity detector (TCD). Water formed during the reduction was captured with a dry ice/isopropanol cold trap.

Inductively coupled plasma (ICP) spectrometry was performed to establish the weight loading of nickel on silica using a Thermo Jarrell Ash model ICAP 61E trace analyzer inductively coupled plasma atomic emission spectrometer (ICP-AES).

Transmission electron microscopy (TEM) measurements were performed on a Talos F200X (200 kV acceleration voltage), operated in TEM mode. A Super-XTM EDX detector included in the machine was used to collect TEM EDX spectra which were quantified using TIA software. Typical analysis was performed by spreading the beam around a suitable area of the sample and using acquisition times of around 5−10 min. The percentage weight loadings of the samples determined by EDX analysis were complemented with ICP measurements. Particle size distributions were obtained by measuring between 100 and 200 particles by hand using ImageJ analysis software.

In situ TEM measurements were performed using a Protochips Atmopshere system. Unless stated otherwise, gasses are introduced at 1 bar pressure to prevent leakage into the lines with a 0.1 sccm flow rate. Measurements under inert atmosphere were performed under argon, and measurements under reducing atmosphere were performed under a mix of 5% H_2/Ar. All gasses were of purity grad N7.0 and all lines were leak checked by evacuating them to 0.1 mbar and measuring the increase in pressure over the course of 10 min prior to each experiment. All line leaks were maintained below 0.001 sccm. Additionally, all experiments were performed at slight overpressure to prevent any leaks into the line. Samples were prepared by drop-casting a sonicated dilute sample dispersed in ethanol onto the chip. Details of the workflow procedures of gas and temperature changes during the *in situ* experiments are discussed in more detail in Section 3.

https://doi.org/10.1021/acs.jpcc.3c01117
J. Phys. Chem. C 2023, 127, 7772−7783

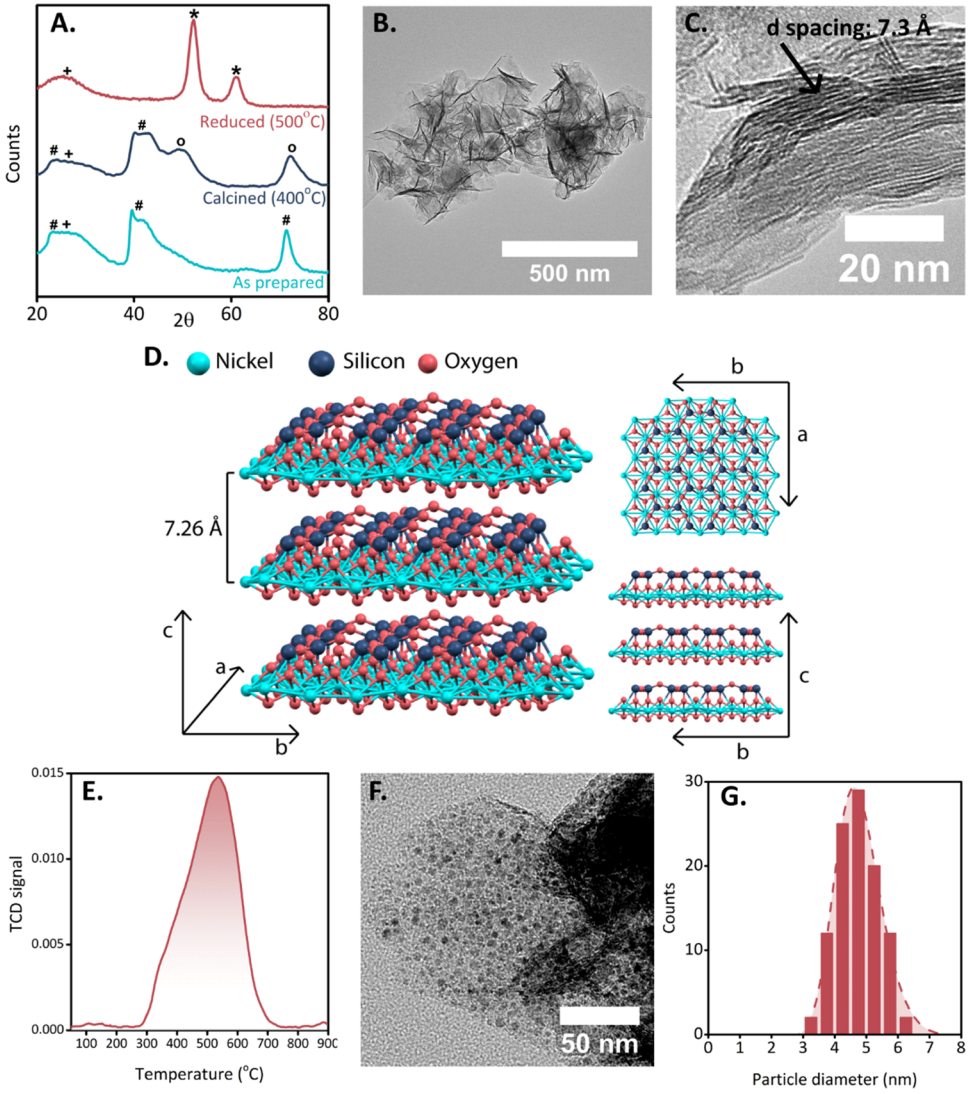

Figure 1. (A) Powder XRD patterns of the as-prepared, calcined, and reduced and passivated samples (+ silica, # phyllosilicate, o nickel oxide, * nickel), (B) TEM image of the as-prepared dried at 120 °C nickel phyllosilicate, and (C) high-resolution TEM image of the as-prepared nickel phyllosilicates. (D) Model of the crystal structure of nickel phyllosilicates. (E) TPR (5 °C·min^{-1}) of the reduction of the as-prepared nickel phyllosilicate. (F) TEM image of the nickel phyllosilicate dried at 120 °C overnight then calcined for 2 h at 400 °C then reduced at 500 °C for 2 h under 5% H_2/Ar flow followed by passivation. (G) Particle size distribution associated with (F).

3. RESULTS AND DISCUSSION

3.1. Characterization of Samples Prepared Ex Situ. A nickel phyllosilicate catalyst precursor was prepared by deposition precipitation based on literature procedures using the urea method and was subsequently characterized with a variety of ex situ techniques to ascertain its composition and structure.[7,27,28] Powder X-ray diffraction (Figure 1A) shows that the as-prepared catalyst precursor was composed of two phases, unreacted amorphous silica (broad peak at 28° labeled +) and 1:1 nickel phyllosilicate (peaks at 22, 40−44, and 71° labeled #). The presence of two phases was expected since both ICP (31%) and EDX (32%) indicated approximately a 30% nickel weight loading on the silica. No other nickel phases could be identified from the X-ray diffractogram. The nickel phyllosilicate and unreacted silica were clearly identifiable in the TEM images of the as-prepared nickel phyllosilicate (Figure 1B,C). The unreacted silica maintains the same morphology as the precursor silica as spheres of 20−200 nm in diameter (Figure S1A). The nickel phyllosilicate can be identified as the "leaf-like" layered material coating the unreacted silica. The d-spacing of this material is consistent with that of 1:1 nickel phyllosilicate.

The morphology of the nickel phyllosilicate catalyst precursor was characterized further as being "leaf-like". The asymmetry of the peak at 40−44° corresponding to the 110 miller plane can be attributed to the two-dimensional (2D) structure of the nickel phyllosilicates as it corresponds to the direction of the stacking of the layers (*c* axis in Figure 1D). Nitrogen physisorption of the as-prepared catalyst precursor shows a significant increase in the surface area from 47 $m^2 \cdot g^{-1}$ for the silica support to 197 $m^2 \cdot g^{-1}$ for the nickel phyllosilicate (Table S1). The physisorption profile of the unreacted silica shows very little hysteresis typical of a support material consisting of large spherical particles with limited mesoporosity from the interparticle space (Figures S1A and S2A,B). In contrast, the as-prepared nickel phyllosilicate physisorption profile shows a large hysteresis in a shape characteristic of materials composed of platelets and thus having narrow slit-

https://doi.org/10.1021/acs.jpcc.3c01117
J. Phys. Chem. C 2023, 127, 7772−7783

shaped pores (Figure S2C,D). From the specific surface area of 197 $m^2 \cdot g^{-1}$, we calculate an average thickness of the layers of 3.2 nm corresponding to approximately 4.5 layers in the c axis of phyllosilicate crystal structure (Method S1).

After calcination at 400 °C for 4 h, characterization by XRD exhibits a new peak at 49° and the peak at 71 shifts to 73°, indicating the formation of some nickel oxide (Figure 1A, labeled o). The morphology of the nickel catalyst precursor remained unchanged from TEM imaging (Figure S1B). The nitrogen physisorption profile confirms that calcination had a negligible effect on the morphology of the catalyst precursor Figure S2E,F.

Subsequent reduction of the sample studied using TPR shows a single broad peak between 300 and 700 °C corresponding to the conversion of nickel phyllosilicate to nickel and silica (Figure 1E). TEM images of the reduced sample show that nanoparticles of nickel had been formed on the silica (Figure 1F). The particle size distribution is shown in Figure 1G with an average particle size of 4.7 ± 0.7 nm. The for mation of the crystalline nanoparticles of metallic nickel was confirmed by XRD (Figure 1A). The BET surface area of the reduced catalyst was 145 $m^2 \cdot g^{-1}$ (Table S1). This loss in surface area can be attributed to the loss of porosity and closer packing of the platelets. Despite this shrinkage both the nitrogen physisorption and the TEM images show that the sample had maintained its leaf-like structure (Figures 1F and S2G,H).

3.2. Evaluating Conditions for the *In Situ* TEM Experiments. A number of experiments were performed in order to establish the optimal conditions for the in situ experiments and to minimize beam effects. The first set of experiments was aimed at establishing the reduction temperature required for the formation of nanoparticles. Although TPR provided the range of temperatures at which the reduction reaction takes place, it provides no direct information on the temperature at which particle formation starts under steady-state conditions. The sample was reduced *ex situ* in a tube furnace at a range of temperatures for 2 h under 1 bar of 5% H_2/Ar flow. TEM images of these samples showed that particles only appeared when the reduction temperature exceeded 450 °C (Figure S3). Reduction at 425 °C for 2 h did not lead to any detectable particle formation (resolution TEM images ~1 nm).

Next, the sample was reduced *ex situ* in a tube furnace but first drop-cast onto a silicon nitride gas cell chip to check that the dispersion of the sample on a chip did not affect the particle size and distribution. This also enabled the *in situ* conditions of high excess of hydrogen relative to the sample and negligible intraparticle diffusion limitations to be approximated in an *ex situ* reactor. The reduction was performed under 1 bar of 5% H_2/Ar at 700 °C with a 5 °C·min^{-1} ramp rate and a 2 h dwell time. The particle sizes and distributions were then established through TEM measurements of the sample on this chip (Figure S4A,B). The final particle size distribution was identical to that obtained using reduction in the tube furnace with a fixed-bed configuration confirming that the dispersion on a silicon nitride window did not affect the reaction.

To compound this finding, the reduction was performed in the gas cell inside the electron microscope under 1 bar 0.1 sccm 5% H_2/Ar at 700 °C with a 5 °C·min^{-1} ramp rate without illumination by the beam during the reduction. The resulting morphology and particle size distribution obtained from images taken at room temperature under 4 mbar of Ar are provided in Figure S4C,D. The particle size distribution was again unaffected; hence, it could be established that the different hydrodynamics of the gas cell had a negligible effect on the reduction of the nickel phyllosilicate over the course of 2 h.

The next set of experiments was aimed at establishing the stability of the as-prepared catalyst precursor under the beam inside the gas cell under an inert atmosphere. In order to do so the sample was illuminated with an electron dose of 10 $e^- \cdot A^{-2} \cdot s^{-1}$ for 5 min under 1 bar pressure of Ar with a 0.1 sccm flow for 5 min at different temperatures. TEM images were acquired throughout and the before and after images can be seen in Figure 2. Significant damage was observed at room temperature although a slight improvement was observed when using low gas pressures of ca. 4 mbar and/or higher flow rates. As the temperature was increased before exposure to the beam, the amount of damage to the sample was reduced. After flowing Ar gas for 5 min at 300 °C, the sample appears to be stable under the electron beam at that temperature.

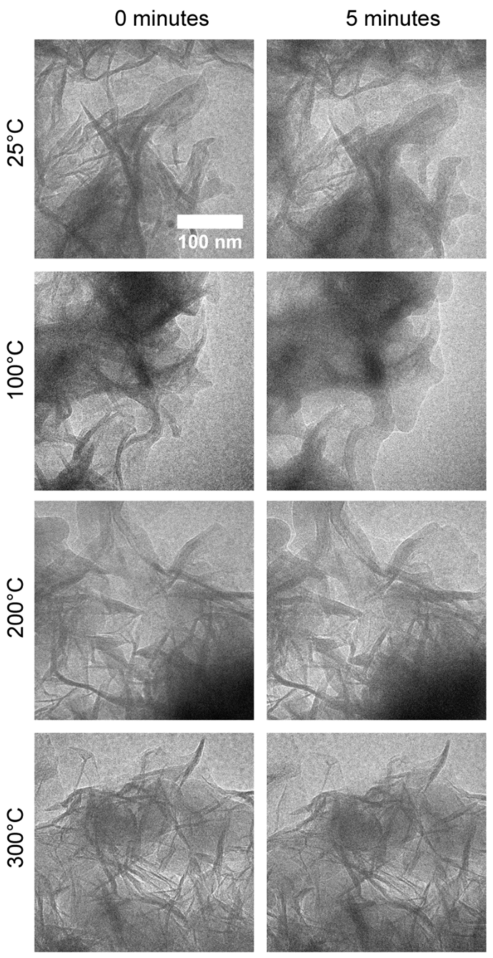

Figure 2. Images of nickel phyllosilicates under 1 bar of Ar gas with a 0.1 sccm flow before and after 5 min of irradiation with an electron dose of 10 $e^- \cdot A^{-2} \cdot s^{-1}$. The images were taken at room temperature, 100, 200, and 300 °C, and the stability of the material can be seen to improve with increasing temperature.

An important conclusion was drawn from this experiment about the stability of the nickel phyllosilicate inside the gas cell under the electron beam. The damage observed is proposed to

https://doi.org/10.1021/acs.jpcc.3c01117
J. Phys. Chem. C 2023, 127, 7772−7783

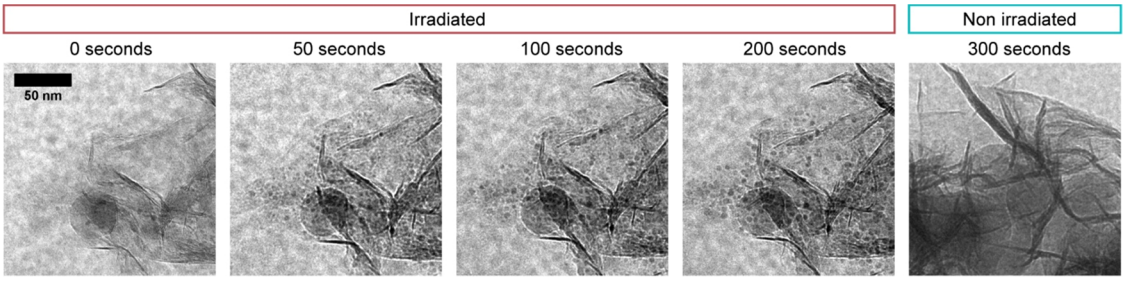

Figure 3. Images acquired during the reduction of nickel phyllosilicates *in situ* under 1 bar of 5% H_2/Ar gas with a 0.1 sccm flow at 425 °C with an electron dose of 30 $e^{-}{\cdot}A^{-2}{\cdot}s^{-1}$ showing the nucleation and growth of nanoparticles only in the presence of the electron beam.

be due to the hydrolysis of siloxane bonds, as has been observed in the literature.[29−31] This hypothesis explains the reduced damage under lower pressures or higher flow rates as the water would be removed more easily from the surface of the sample. Increasing the temperature and essentially performing a drying step prior to imaging removes these effects entirely. Imaging the sample at a temperature of above 300 °C in Ar gas causes no observable damage to the material which maintains its morphology and its crystallinity as confirmed by the unaltered lattice spacings in the phyllosilicate sheets. Therefore, for all subsequent experiments, the sample was dried *in situ* at 300 °C under a flow of argon for at least 40 min prior to any exposure to the electron beam.

The last set of what one may consider as "control" experiments were aimed at establishing the temperature for the reduction of the sample *in situ*. To do so, the sample was first dried *in situ* at 300 °C for 45 min before being exposed to 1 bar of 5% H_2/Ar gas at a 0.1 sccm flow and imaged. The temperature was then increased incrementally until particles were seen to form under the beam. No particles (resolution approximately 1 nm) were observed until a temperature of 425 °C was reached. Images from this experiment are shown in Figure 3. These nanoparticles formed only in areas illuminated by the beam, images of nonirradiated areas showed no nanoparticle formation. *Ex situ* reduction at 425 °C in earlier experiments did not lead to any particle formation (Figure S3B). From this, it could be established that the electron beam did affect nucleation of nanoparticles at the prevailing conditions.

Previous studies on the reduction of nickel phyllosilicates have shown that the particle size formed during the reduction is only weakly dependent on temperature in between 500 and 900 °C, due to the strong interaction of the particles with the support.[33] It was decided that in order to minimize the effect of the beam-induced nucleation of the nanoparticles, a higher temperature should be used. The temperature of 600 °C was chosen as the thermal energy provided to the system was sufficient to enhance nucleation and growth rates to be much greater than those induced by the electron beam. This is expected to make the impact of the electron beam on the system negligible relative to the effect of the temperature and therefore provide meaningful particle growth curves. The results of the reduction at 600 °C are shown in Figure S5. At 600 °C the particles formed rapidly, with nucleation occurring within 3 s and growth terminating after 25 s. Immediate imaging of a nonirradiated area after the 200 s of the experiment shows that particles of the same size and distribution are formed as seen in the irradiated areas. Particle size distributions from both irradiated and nonirradiated areas have a negligible difference. The rate of the reaction means that the sample shrinks rapidly and the resolution of the images is reduced due to the movement of the sample. As a result of this experiment, the reaction temperature of 500 °C was chosen for the detailed in situ experiments. The lowering of the temperature by 100 °C slowed the particle growth somewhat and made collecting good-quality images of the reduction process possible. The chosen temperature of 500 °C represents the center of the reduction peak for nickel phyllosilicates (Figure 1E) and is a temperature at which there is enough thermal energy delivered to the sample to render the energy contribution of the electron beam insignificant. Additionally, the use of lower reduction temperatures is often preferable in an industrial context for reasons of safety and cost, and has been known to increase the activity of such catalysts.[32] The experiments presented show that reduction at 500 °C compared to 600 °C increases the time of particle nucleation and growth from 25 to 180 s. This increase in particle growth time is insignificant when considering that reduction of this material in the literature is usually performed for lengths of time consisting of hours rather than minutes.[33] As such, we believe that this choice of temperature remains relevant and has the potential to guide others in the choices of temperatures and lengths of time needed to reduce such catalyst precursors.

Two *in situ* experiments were designed to study the reduction of nickel phyllosilicates at 500 °C, the first over the course of 15 min with an image acquired every 30 s to study the overall particle growth (experiment 1), and the second for 3 min with a high frame rate of 4 images per second to study the early stages of particle growth (experiment 2). A schematic representation of the design of these experiments is provided in Figure 4 showing not only the temperature and pressures that the sample was exposed to and the times of illumination. The samples were all dried for at least half an hour inside the gas cell at 300 °C under 1 bar Ar, 0.1 sccm flow prior to any exposure to the beam. In both experiments, the samples were briefly illuminated after this drying step for the purpose of focusing and finding suitable areas for imaging. This exposure to the beam was always at a dose rate of under 30 $e^{-}{\cdot}A^{-2}{\cdot}s^{-1}$ and for no longer than 60 s. The beam was then blanked as the gas was switched to 1 bar of 5% H_2/Ar at a 0.1 sccm flow, maintaining the temperature still at 300 °C which is well below the reduction temperature of the nickel phyllosilicates. The sample was then further illuminated for a maximum of 30 s as the switching of gasses always causes a minor shift in the position of the stage and focus and requires some readjustments of the microscope. For both experiments, the imaging then commenced as the temperature ramp of 10 $°C{\cdot}s^{-1}$ begins, which means that within the first 20 s of imaging the sample reaches the desired temperature of 500 °C. For both experiments, the sample was exposed to the beam

https://doi.org/10.1021/acs.jpcc.3c01117
J. Phys. Chem. C 2023, 127, 7772−7783

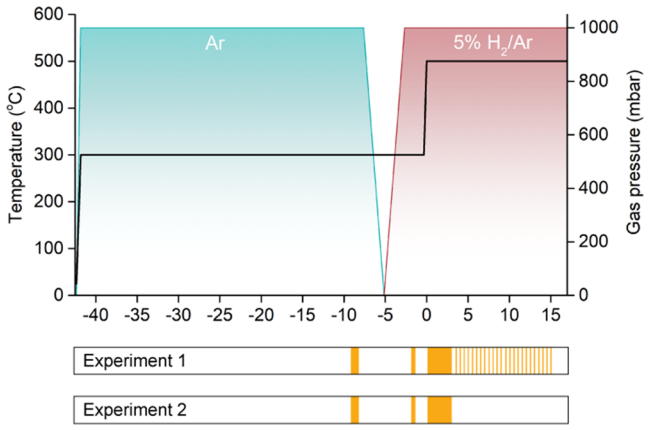

Figure 4. Schematic representation of the procedure used for the *in situ* experiments including gasses, temperature, and irradiation times. The plot illustrates the temperature and pressure of the gas cell system as a function of time with time $t = 0$ being the time at which the recording of the reduction experiment began. The bars beneath the plot labeled Experiment 1 and Experiment 2 illustrate the illumination times of the sample during each experiment, where the yellow regions indicate that the sample is illuminated for that time period. A drying step is performed first under 0.1 sccm of argon gas at 300 °C for 45 min with no irradiation by the electron beam. At the end of this drying, the region of interest is identified and the sample is irradiated for a few minutes at time $T = -10$. Then, the gas is switched to 5% H_2/Ar, which causes minor movement of the sample holder and the sample is then illuminated briefly again to refocus and find the region of interest again at $T = -3$. Then, the imaging settings are finalized and set up. At $T = 0$, the experiment starts in earnest and the temperature is rapidly increased to 500 °C.

continuously for the first 3 min of the reaction. For the short-time experiment (experiment 2), this constitutes the whole time of exposure with an imaging rate of four images per second. For experiment 1 the first 6 images were collected 30 s apart with continuous illumination, the beam was then blanked between the remaining images taken 30 s apart for 15 min. Immediately after the recording of the reduction was terminated, another location on the grid was found that had not previously been exposed to the beam and was imaged for comparative purposes.

3.3. Results of *In Situ* Experiments. Experiment 1 provided valuable information on the timescale of nanoparticle growth during the reduction of the nickel phyllosilicates. The experiment lasted 15 min and an image was acquired *in situ* in the electron microscope every 30 s during the reduction at 500 °C static temperature under a flow of 0.1 sccm of 1 bar of 5% H_2/Ar. The sample was irradiated continuously for the first 3 min. Thereafter the electron beam was blanked in between image acquisitions. The electron dose was maintained below 30 $e^{-}\cdot A^{-2}\cdot s^{-1}$ throughout. Images from experiment 1 can be seen in Figure 5 and correspond to Video 1 (Supporting Information). The sample appeared to no longer change from around 3 min of reaction time suggesting that the particle growth was complete.

To confirm this finding, the particle sizes from the images were measured for 76 particles and the histograms of particle diameters used to calculate the average particle sizes are provided in Supporting Information Figure S6. The plot of the average particle size as a function of time in Figure 5 shows that after 3 min, the average particle size is stable. The majority of the nucleation and growth takes place within the first 3 min of the reaction.

Imaging of a nonirradiated area within the first 2 min after completion of experiment 1 was performed to establish that the reaction had taken place homogeneously across the chip (Figure 5). The average particle size and the corresponding particle size distribution from the nonirradiated area do not differ significantly from that of the irradiated area. It was impossible to tell whether the nucleation of the particles was triggered by exposure to the electron beam in the irradiated area; as a result, we cannot comment on the nucleation times of the particles. We propose that the subsequent particle growth is assumed to be representative of that which is occurring in the nonirradiated areas.

Although experiment 1 demonstrated that the growth of the particles in the gas cell is a very rapid process, it was important

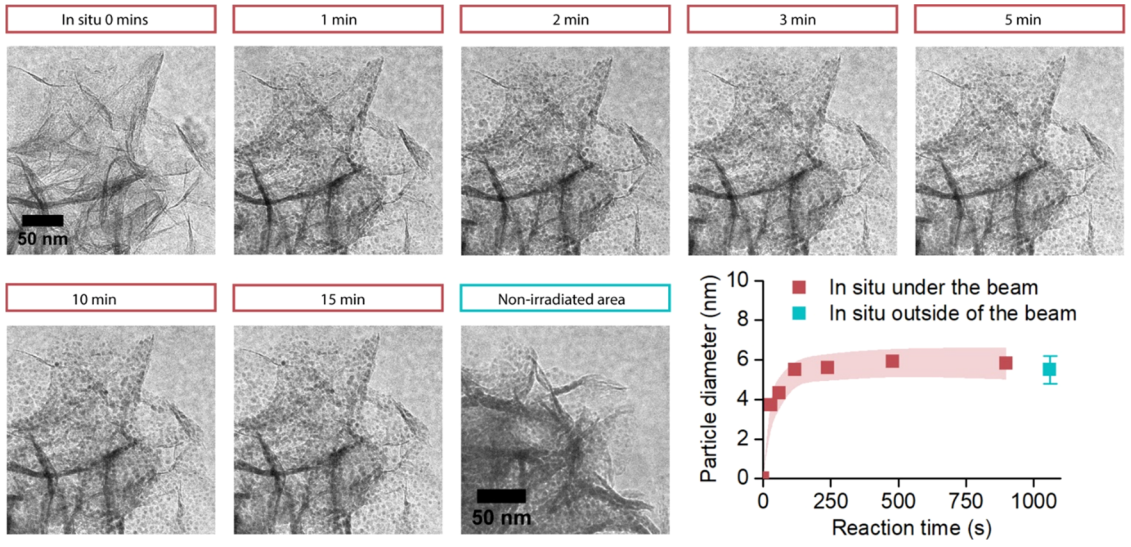

Figure 5. *In situ* TEM images acquired during experiment 1 under 1 bar of 5% H_2/Ar with a flow of 0.1 sccm at 500 °C with an electron dose rate below 30 $e^{-}\cdot A^{-2}\cdot s^{-1}$. An image of a nonirradiated area is provided for comparison, and the average particle sizes from the images are plotted to demonstrate the particle growth.

https://doi.org/10.1021/acs.jpcc.3c01117
J. Phys. Chem. C 2023, 127, 7772−7783

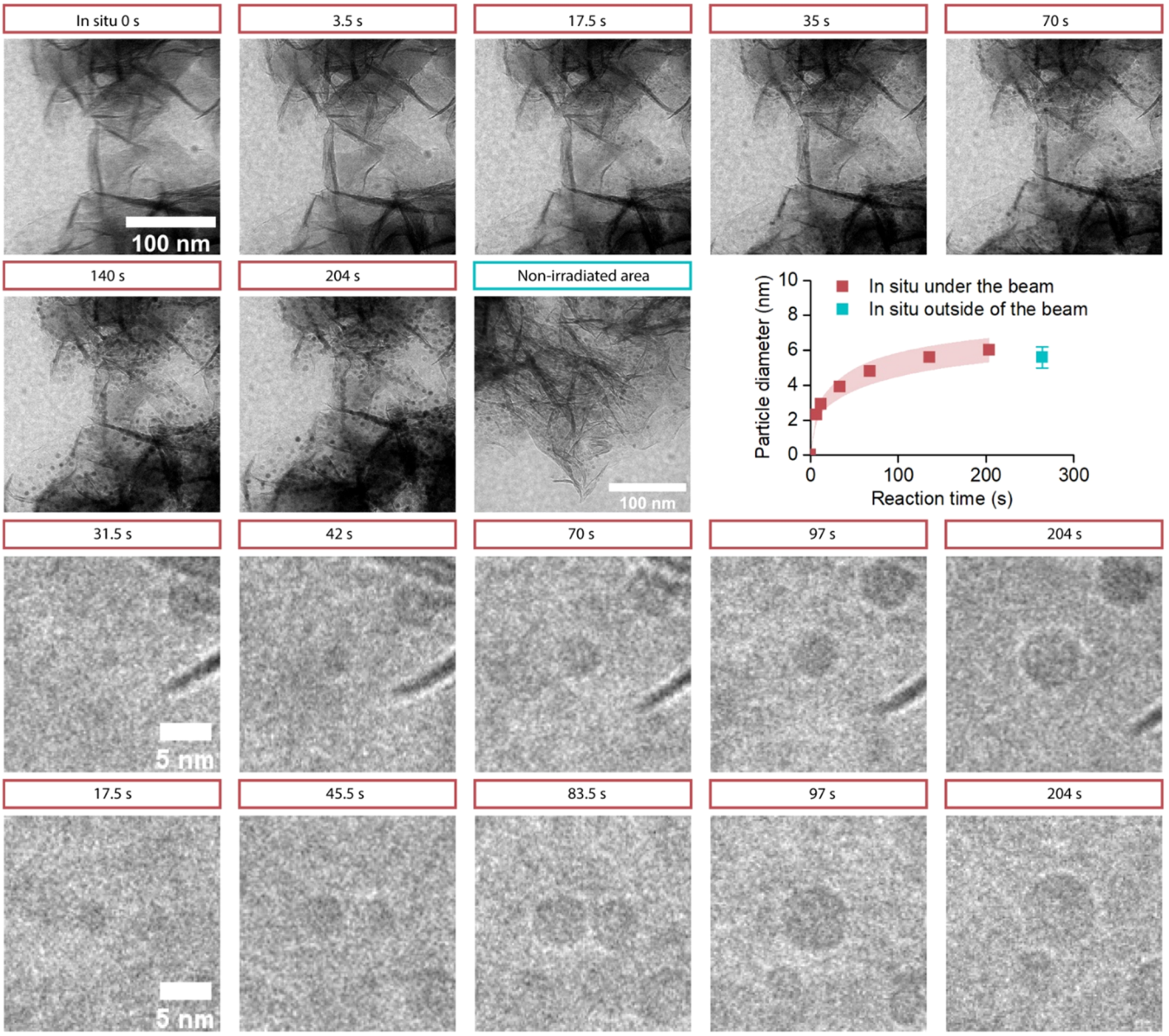

Figure 6. Rows 1 and 2: *in situ* TEM images acquired during experiment 2 under 1 bar of 5% H_2/Ar with a flow of 0.1 sccm at 500 °C with an electron dose rate below 30 $e^{-}{\cdot}A^{-2}{\cdot}s^{-1}$, an image of a nonirradiated area is provided for comparison, and the average particle sizes from the images are plotted to demonstrate the particle growth; row 3: close-up of a particle experiencing growth, row 4: close-up of two particles experiencing sintering after growth.

to ascertain whether or not the sample was fully reduced. This was tested by increasing the temperature further to 700 °C for a further 20 min. The higher temperature and longer time triggered no further increase in the particle size suggesting that the reduction was finished after 3 min at 500 °C.

This surprising finding contrasts with *ex situ* reduction experiments such as TPR where at least 40 min were required to fully reduce the sample. These differences are likely due to differences in the diffusion rates and therefore compositions of gasses to and from the sample in the two systems. *Ex situ* TPR experiments are performed in plug flow reactor setups where significantly larger amounts of sample are analyzed. This means that the ratio between H_2 gas and the sample to be reduced is much lower *ex situ* than *in situ*. The diffusion of the gas to and from the sample is also significantly enhanced in a gas cell setup relative to a plug flow reactor configuration. In the gas cell, where the sample is dispersed in a very thin layer on the chip, there are no intraparticle diffusion limitations. A most important consequence is the build-up of water in the gas stream ex situ. Water is known to significantly slow reduction processes, and as it is the product of the reduction of the nickel phyllosilicate it builds up in the gas stream as the gas passes through the sample in a plug flow reactor configuration.[27,28] In the case of nickel phyllosilicate reduction, the flow rates of gasses and partial pressure of water in the gas stream are known to be the primary factor controlling the eventual particle size[33] This effect is negligible in the in situ gas cell configuration and points to the decisive role of the gas composition in the reduction kinetics in bulk reactors.

It is therefore notable that the conclusion that the particle growth takes place in around 3 min can only be assumed to apply to the ideal dry conditions with no gas diffusion limitations and a large excess of hydrogen. Further studies would be required to establish the particle growth kinetics in

https://doi.org/10.1021/acs.jpcc.3c01117
J. Phys. Chem. C 2023, 127, 7772−7783

the presence of water in the gas stream, or where gas diffusion limitations come into play, or if there are lower concentrations of hydrogen available. It is also notable that the finding that the time frame of particle growth is a factor of 10 smaller (3 vs 40 min) than the time frame of *ex situ* reduction in the TPR is in stark contrast with a similar study performed by van den Berg et al.[31] on the reduction of copper phyllosilicates in an ETEM configuration under 1 mbar of static gas. In their work, the copper phyllosilicate was reduced in a time frame of 20 min in the TPR and TGA experiments *ex situ* and the particle growth occurred within a time frame of 25 min in their *in situ* study, representing a good match between the *ex situ* and *in situ* experiments, despite the fact that the reduction environments were less comparable.

Although the 15 min experiment 1 yielded valuable information on the growth rate of the particles, the growth was fast and difficult to study with 30 s intervals. For this reason, a shorter time period experiment was run at a higher magnification in order to study in more detail the growth process. The images from experiment 2 were recorded at a rate of 4 per second to capture as best as possible the changes taking place to the material and were recorded for the first 200 s of the reaction. Some of these images are presented in Figure 6 alongside a plot of the average particle size over time and an image of a nonirradiated area. The particle sizes from the images were measured for 40 particles and the histograms used to calculate the average particle sizes are provided in Supporting Information Figure S7. Although more than 40 particles were in the field of view during the experiment, many overlapped with one another or the support material, raising the risk of having inaccurate particle size measurements if included in the fittings. As such only particles that could be clearly followed from nucleation through to the end of their growth are reported here to maximize the quality of the data. The associated video can be found in the Supporting Information (Video 2).

From the average particle size plot, it can be seen that after 200 s the growth of the nanoparticles was incomplete; however, from experiment 1, it is known that these nanoparticles did not change significantly beyond this time. A plot overlaying the average particle growth curves from both of these experiments shows that they are in agreement with one another (Supporting Information Figure S8). A closer observation of the growth of single particles from this data revealed surprising information about the mechanism of particle growth. Although the majority of the particles grew steadily from their nucleation time, those in close proximity to one another sintered. Close-ups of particles displaying both of these growth mechanisms are shown in Figure 6 and in the videos in the Supporting Information (Videos 3 and 4).

By measuring the diameter of the particles labeled in Figure 7 as a function of time, the growth of individual particles could be plotted and modeled (Figure 8). The growth curves suggest that the model for particle growth is consistent with that described by van den Berg et. al. wherein nickel species are reduced in a region surrounding a nucleation point from which a particle will grow until that region is depleted.[31] Once the surrounding region is depleted the particle size becomes stable and ceases to grow. This is exemplified by particle 5 and particle 32, which have a small number of nearest neighbors and reach large sizes (6.4 and 6.2 nm, respectively). This is in contrast to particles such as particle 9 and particle 16, which have a larger number of neighbors, and although nucleate at a

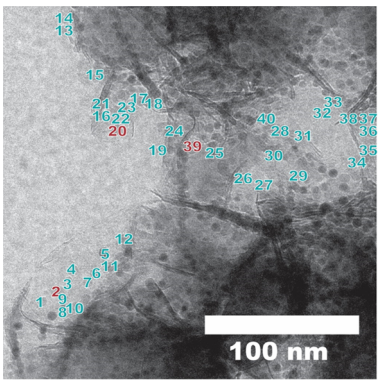

Figure 7. Final image acquired during experiment 2 where the particles for which the growth was tracked in detail and modeled are labeled with numbers. The particles that experienced sintering are labeled in red.

similar time to particle 5 and particle 32, only reach 5.1 and 5.2 nm, respectively. This suggests that the final size of the particles would be predominantly influenced by the synthesis of the phyllosilicate sheets themselves, for example, the thickness of the sheets, their interconnectivity, and the number of defects that may enhance nucleation, as well as the mobility of the nickel species in the region surrounding the nucleation site. From the literature, we know that particle size is dependent on the water concentration of the gas stream.[33] It may be possible to further tune the particle size by modifying the structure and homogeneity of the nickel phyllosilicate sheets.

Analysis of the particle growth curves for those that undergo sintering showed that although slightly larger particle sizes are obtained (6.8 nm for particle 4, 6.7 nm for particle 39, and 6.4 nm for particle 20), they are not unusually larger than particles that grow without experiencing sintering (for example particle 36 is 6.9 nm and particle 18 which reaches 6.6 nm). This is demonstrated in Figure 9 where the range of final sizes of the particles that undergo sintering is overlayed onto the final particle size distribution histogram. Additionally, the particles for which sintering is exhibited in these growth curves are only those for which the full nucleation and growth could be clearly seen and therefore measured in the footage. Others were identified where sintering was observed but particle sizes under 5 nm were obtained, although the early growth stages were too unclear to measure accurate particle sizes due to overlapping sheets. Again, this phenomenon can be explained through the particle growth mechanism suggested by van den Berg et al. for the reduction of copper phyllosilicates.[31] It assumes that the nickel available for particle growth comes from a set region in the vicinity of the nucleation point. Therefore the limiting factor determining the final particle size is the size of the domain from which this nickel is accumulated. If two nucleation points appear within close enough proximity to one another such that it would be possible for them to touch during their growth, the size of the region from which the nickel originates would not be significantly different from that for a single nucleation point.

A final point of interest is the identification of occurrences of late nucleation. From the data collected here, 60% of the particles measured nucleated within the first 30 s of the experiment, and 80% within the first 60 s. The particles that appear late such as particles 11, 22, 28, and 37 can do so surprisingly late: 124, 151, 110, and 111 s, respectively. These

https://doi.org/10.1021/acs.jpcc.3c01117
J. Phys. Chem. C 2023, 127, 7772−7783

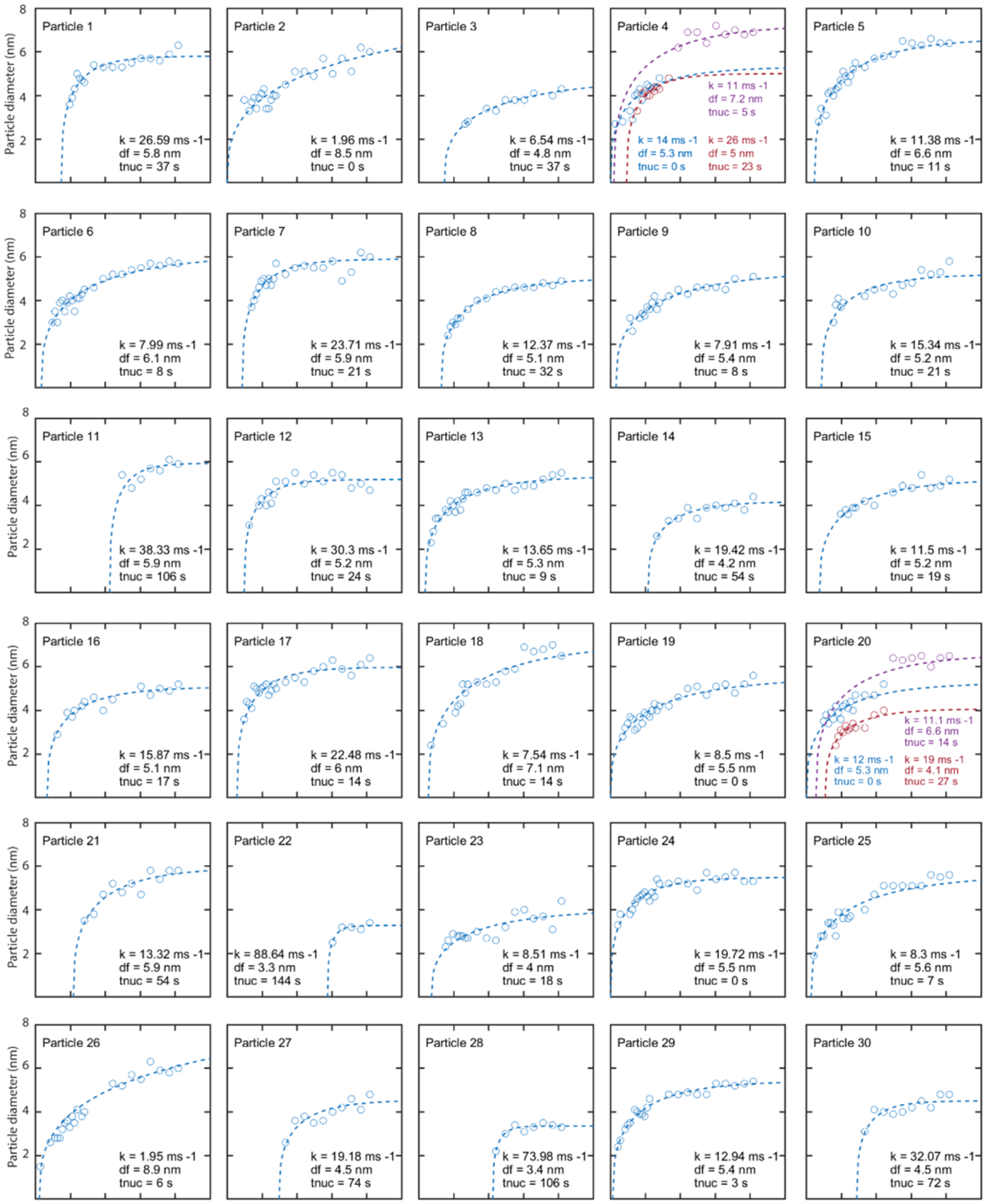

Figure 8. continued

https://doi.org/10.1021/acs.jpcc.3c01117
J. Phys. Chem. C 2023, 127, 7772−7783

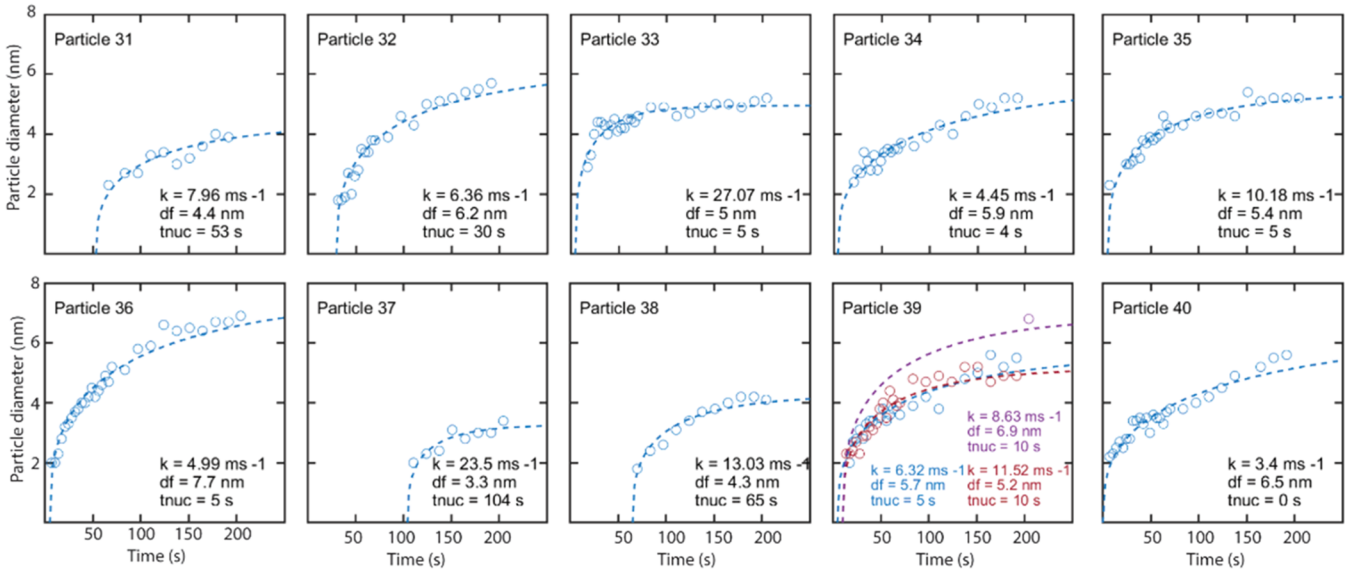

Figure 8. Individual particle growth curves associated with the 40 particles labeled in Figure 7 plotted with the time of reaction in seconds on the x axis and the measured particle diameter in nm on the y axis. The curves are fitted with the first-order kinetic model described in this paper, and the fit parameters are provided for each plot where k is the rate constant, d_f is the final particle size, and tnuc is the time of nucleation.

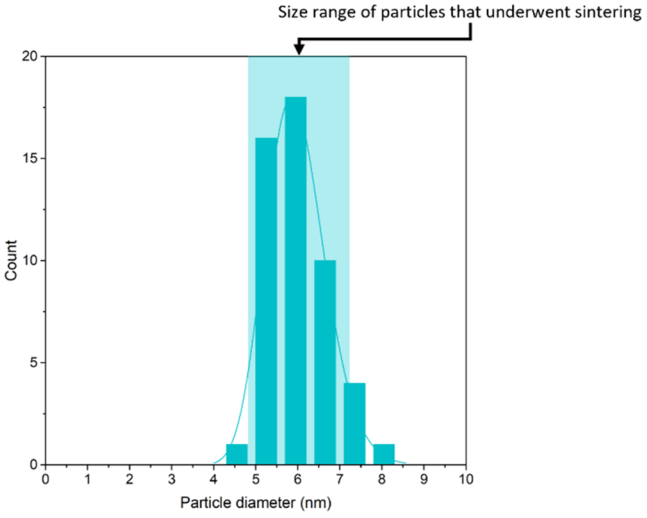

Figure 9. Histogram of final particle sizes obtained after experiment 2 with the region in red highlighting the size range of particles that underwent sintering.

particles appear rapidly, and their size stabilizes almost immediately suggesting that their growth is accelerated relative to their neighbors. It is possible that these particles experience a form of catalyzed growth due to the build-up of large amounts of metallic nickel in their vicinity. Considering the similarity in the findings thus far with respect to the work of van den Berg et al., attempts were made to use the same autocatalytic diffusion and reaction-limited models to fit the individual particle growth curves obtained in Figure 8.[31] Unfortunately the sharp growth and sudden plateau of the nanoparticle size seen in the formation of the copper particles did not appear in the study of the nickel particles. Instead after some trial and error, it was found that a first-order kinetic model produced the best and simplest fits for the nickel particle growth from a phyllosilicate precursor. The particle growth curves were modeled here with the assumption that the growth of the nanoparticle (i.e., rate of formation of Ni^0 as a function of time (t)) is first order with respect to the initial concentration of the Ni^{2+} at $t = 0$. The following expression was obtained:

$$[Ni^0]_{(t)} = [Ni^{2+}]_{(t=0)} \times (1 - e^{-kt})$$

This can be converted to an expression for the diameter $d_{(t)}$ of the nanoparticle over time when assuming that the final diameter of the nickel particle is proportional to the amount of Ni^{2+} in the nickel phyllosilicate reservoir. The diameter can therefore be expressed as follows and fitted for the parameters d_f the final size of the nanoparticle, k the rate constant of the particle growth, and tnuc the time of nucleation of the particle.

$$d_{(t)} = d_f \times (1 - e^{-k(t-\text{tnuc})})^{1/3}$$

The fitting parameters were confined to certain boundary conditions: d_f had to be more than 90% of the largest measured size of the particle, tnuc must fall between 0 and the earliest measured time at which the particle was visible, and k must be a positive number. The nucleation time was the only parameter to occasionally fit to its boundary condition of $t = 0$; however, it is possible the nucleation occurred immediately at $t = 0$ due to the sudden exposure to the electron beam so these fits were still deemed reliable. The obtained rate constants are all between 2 and 89 s^{-1} with an average value of 17 s^{-1} (Figure S9), over 90% of the particles grow with rate constants between 2 and 30 s^{-1}. Only four outlier particles have growth rates above 30 s^{-1}, all four are particles that nucleate late and exhibit the aforementioned catalyzed growth, namely, particles 11, 22, 28, and 30. Particles that undergo sintering processes all have growth rates within the normal range suggesting that the proximity of two nucleation points has no significant effect on the growth rate of the particles. Energies of activation of the particle nucleation and growth cannot be extracted from these experiments at only a single temperature; however, it is hoped that further studies at a broader range of temperatures using a similar methodology will be able to provide more insight into the future.

https://doi.org/10.1021/acs.jpcc.3c01117
J. Phys. Chem. C 2023, 127, 7772−7783

4. CONCLUSIONS

The establishment of appropriate conditions for the *in situ* reduction of nickel phyllosilicates enabled the growth of individual nanoparticles to be studied using TEM. It was revealed that under these conditions (500 °C and 1 bar of 5% H_2 in Ar, 0.1 sccm flow), particle growth takes place rapidly, with growth completed within the first 3 min of the temperature reaching 500 °C.

A two-step particle growth mechanism was observed. First particles grow steadily, and then if sufficiently close to one another they can sinter. This process did not lead to significantly larger nanoparticles than those which did not undergo sintering. This enabled the conclusion to be drawn that the limiting factor in the final particle size for these catalysts is the size of the region from which the nickel is sourced. The size of this region is likely to be affected by the synthesis of the phyllosilicate itself, for example, the thickness of the sheets, their defect concentration, and their interconnectivity providing avenues for further research into controlling the particle sizes and distributions for these catalysts. Late nucleation was observed as a rare event and led to more rapid growth and smaller particle sizes relative to earlier nucleation times.

■ ASSOCIATED CONTENT

Supporting Information

The Supporting Information is available free of charge at https://pubs.acs.org/doi/10.1021/acs.jpcc.3c01117.

Additional TEM images of the materials studied, information about the porosity and surface areas of the materials alongside the method used to calculate the thickness of the nickel phyllosilicate sheets, and additional results from preliminary experiments used to establish the correct conditions for the in situ experiments reported and discussed herein (PDF)

Experiment 1 (Video 1) (AVI)

Experiment 2 (Video 2) (AVI)

Particles displaying both typical particle growth and a secondary sintering event (Video 3) (AVI)

Particles displaying typical particle growth (Video 4) (AVI)

■ AUTHOR INFORMATION

Corresponding Author

Krijn P. de Jong − *Materials Chemistry and Catalysis, Debye Institute for Nanomaterials Science, Utrecht University, 3584 CG Utrecht, The Netherlands;* orcid.org/0000-0002-9773-8110; Email: K.P.deJong@uu.nl

Authors

Savannah J. Turner − *Materials Chemistry and Catalysis, Debye Institute for Nanomaterials Science, Utrecht University, 3584 CG Utrecht, The Netherlands;* orcid.org/0000-0002-7228-2110

Dennie F. L. Wezendonk − *Materials Chemistry and Catalysis, Debye Institute for Nanomaterials Science, Utrecht University, 3584 CG Utrecht, The Netherlands*

Robert J. A. M. Terorde − *BASF Nederland B.V., 3454 PK Utrecht, The Netherlands*

Complete contact information is available at: https://pubs.acs.org/10.1021/acs.jpcc.3c01117

Author Contributions

S.J.T., R.J.A.M.T., and K.P.D.J. conceived and planned the experiments. S.J.T. performed the synthesis and characterization of the material. S.J.T. performed the in situ transmission electron microscopy experiments with technical support from D.F.L.W. S.J.T. analyzed the in situ data with support from K.P.D.J. and R.J.A.M.T. K.P.D.J. supervised the work. All authors contributed to the final manuscript.

Notes

The authors declare no competing financial interest.

■ ACKNOWLEDGMENTS

S.J.T. and Prof. K.P.J. gratefully thank B. Reesink, R. Terorde, and I. Yarulina for fruitful discussions and input. S.J.T. acknowledges BASF and the ARC CBBC for funding under project number 2016.005.B.UU.

■ REFERENCES

(1) Eskandari, S.; Tate, G.; Robert, N. R.; Regalbuto, J. R. Nanoparticle Synthesis via Electrostatic Adsorption Using Incipient Wetness Impregnation. *ACS Catal.* **2018**, *8*, 10383−10391.

(2) de Jong, K. P. *Synthesis of Solid Catalysts*; de Jong, K. P., Ed.; Wiley-VCH: Weinheim, 2009; pp 1−11.

(3) Cheng, K.; Smulders, L. C. J.; van der Wal, L. I.; Oenema, J.; Meeldijk, J. D.; Visser, N. L.; Sunley, G.; Roberts, T.; Xu, Z.; Doskochil, E.; et al. Maximizing Noble Metal Utilization in Solid Catalysts by Control of Nanoparticle Location. *Science* **2022**, *377*, 204−208.

(4) Pinna, F. Supported Metal Catalysts Preparation. *Catal. Today* **1998**, *41*, 129−137.

(5) Munnik, P.; de Jongh, P. E.; de Jong, K. P. Recent Developments in the Synthesis of Supported Catalysts. *Chem. Rev.* **2015**, *115*, 6687−6718.

(6) Albarazi, A.; Galvez, M. E.; Da Costa, P. Synthesis Strategies of Ceria−Zirconia Doped Ni/SBA-15 Catalysts for Methane Dry Reforming. *Catal. Commun.* **2015**, *59*, 108−112.

(7) Burattin, P.; Louis, C.; Che, M. Characterization of the Ni(II) Phase Formed on Silica Upon Deposition−Precipitation. *J. Chim. Phys. B* **1997**, *101*, 7060−7074.

(8) Mette, K.; Kuhl, S.; Dudder, H.; Kahler, K.; Tarasoc, A.; Muhler, M.; Behrens, M. Stable Performance of Ni Catalysts in the Dry Reforming of Methane at High Temperatures for the Efficient Conversion of CO2 into Syngas. *ChemCatChem* **2014**, *6*, 100−104.

(9) Marceau, E.; Bonneviot, L.; Dzwigaj, S.; Lambert, J.; Louis, C.; Carrier, X. Interfacial Coordination Chemistry for Catalyst Preparation. *J. Catal.* **2021**, *396*, 104−121.

(10) Che, M.; Bennett, C. *Advances in Catalysis*; Eley, D. D.; Pines, H.; Weisz, P., Eds.; Academic Press,: Cambridge, 1989; Vol. *36*, pp 55−172.

(11) Munnik, P.; Wolters, M.; Gabrielsson, A.; Pollington, S. D.; Headdock, G.; Bitter, J. H.; de Jongh, P. E.; de Jong, K. P. Copper Nitrate Redispersion To Arrive at Highly Active Silica-Supported Copper Catalysts. *J. Phys. Chem. A* **2011**, *115*, 14698−14706.

(12) Mondloch, J. E.; Bayram, E.; Finke, R. G. J. A Review of the Kinetics and Mechanisms of Formation of Supported-nanoparticle Heterogeneous Catalysts. *J. Mol. Catal. A: Chem.* **2012**, *355*, 1−38.

(13) Knozinger, H. *Characterisation of Solid Catalysts*; Ertl, G.; Knozinger, H.; Weitkamp, J., Eds.; Wiley-VCH: Weinheim, 1997; pp 582−689.

(14) Thanh, N. T. K.; Maclean, N.; Mahiddine, S. Mechanisms of Nucleation and Growth of Nanoparticles in Solution. *Chem. Rev.* **2014**, *114*, 7610−7630.

(15) Topsøe, H. Developments in Operando Studies and In Situ Characterization of Heterogeneous Catalysts. *J. Catal.* **2003**, *216*, 155−164.

(16) Haber, J.; Block, J. H.; Delmon, B. *Handbook of Heterogeneous Catalysis*; Ertl, G.; Knozinger, H.; Weitkamp, J., Eds.; Wiley-VCH: Weinheim, 2008; pp 1230−1258.
(17) Su, D. Advanced Electron Microscopy Characterization of Nanomaterials for Catalysis. *Green Energy Environ.* **2017**, *2*, 70−83.
(18) Challa, S. R.; Delariva, A. T.; Hansen, T. W.; Helveg, S.; Sehested, J.; Hansen, P. L.; Garzon, F.; Datye, A. K. Relating Rates of Catalyst Sintering to the Disappearance of Individual Nanoparticles during Ostwald Ripening. *J. Am. Chem. Soc.* **2011**, *133*, 20672−20675.
(19) Takeda, S.; Kuwauchi, Y.; Yoshida, H. Environmental Transmission Electron Microscopy for Catalyst Materials using a Spherical Aberration Corrector. *Ultramicroscopy* **2015**, *151*, 178−190.
(20) Banerjee, R.; Crozier, P. A. In Situ Synthesis and Nanoscale Evolution of Model Supported Metal Catalysts: Ni on Silica. *J. Phys. Chem. C* **2012**, *116*, 11486−11495.
(21) Wu, F.; Yao, N. Advances in Sealed Liquid Cells for In-situ TEM Electrochemial Investigation of Lithium-ion Battery. *Nano Energy* **2015**, *13*, 735−756.
(22) van der Wal, L. I.; Turner, S. J.; Zecevic, J. Developments and Advances in In Situ Transmission Electron Microscopy for Catalysis Research. *Catal. Sci. Technol.* **2021**, *11*, 3634−3658.
(23) de Jonge, N.; Ross, F. Electron Microscopy of Specimens in Liquid. *Nat. Nanotechnol.* **2011**, *6*, 695−704.
(24) Epicier, T.; Rainforth, N. Environmental Electron Microscopy: Materials in their Real Live in Gas or Liquid. *J. Microsc.* **2018**, *269*, 115−116.
(25) Huang, X.; Farra, R.; Schlogl, R.; Willinger, M. Growth and Termination Dynamics of Multiwalled Carbon Nanotubes at Near Ambient Pressure: An in Situ Transmission Electron Microscopy Study. *Nano Lett.* **2019**, *19*, 5380−5387.
(26) Tao, F. F.; Crozier, P. Atomic-Scale Observations of Catalyst Structures under Reaction Conditions and during Catalysis. *Chem. Rev.* **2016**, *116*, 3487−3539.
(27) Hermans, L. A. M.; Geus, J. W. Interaction Of Nickel Ions With Silica Supports During Deposition-Precipitation. *Stud. Surf. Sci. Catal.* **1979**, *3*, 113−130.
(28) van der Lee, M. K.; van Dillen, A. J.; Bitter, J. H.; de Jong, K. P. Deposition Precipitation for the Preparation of Carbon Nanofiber Supported Nickel Catalysts. *J. Am. Chem. Soc.* **2005**, *127*, 13573−13582.
(29) Mølhave, K.; Gudnason, S.; Pedersen, A. T.; Clausen, C. H.; Horsewell, A.; Boggild, P. Electron Irradiation-induced Destruction of Carbon Nanotubes in Electron Microscopes. *Ultramicroscopy* **2007**, *108*, 52−57.
(30) Meijerink, M. J.; Spiga, C.; Hansen, T. W.; Damsgaard, C. D.; de Jong, K. P.; Zečević, J. Nanoscale Imaging and Stabilization of Silica Nanospheres in Liquid Phase Transmission Electron Microscopy. *Part. Part. Syst. Charact.* **2019**, *36*, No. 1800374.
(31) van den Berg, R.; Elkjaer, C. F.; Gommes, C. J.; Chorkendorff, I.; Sehested, J.; de Jongh, P. E.; de Jong, K. P.; Helveg, S. Revealing the Formation of Copper Nanoparticles from a Homogeneous Solid Precursor by Electron Microscopy. *J. Am. Chem. Soc.* **2016**, *138*, 3433−3442.
(32) Kuhaudomlap, S.; Mekasuwandumrong, O.; Praserthdam, P.; Lee, K. M.; Jones, C. W.; Panpranot, J. Influence of Highly Stable Ni^{2+} Species in Ni Phyllosilicate Catalysts on Selective Hydrogenation of Furfural to Furfuryl Alcohol. *ACS Omega* **2023**, *8*, 249−261.
(33) Burattin, P.; Che, M.; Louis, C. Ni/SiO_2 Materials Prepared by Deposition−Precipitation: Influence of the Reduction Conditions and Mechanism of Formation of Metal Particles. *J. Phys. Chem. B* **2000**, *104*, 10482−10489.

https://doi.org/10.1021/acs.jpcc.3c01117
J. Phys. Chem. C 2023, 127, 7772−7783